PHYSICAL SCIENCES

Copyright © 2024 The Authors, some rights reserved; exclusive licensee American Association for the Advancement of Science. No claim to original U.S. Government Works. Distributed under a Creative Commons Attribution NonCommercial License 4.0 (CC BY-NC).

# Robust hybrid diffusion control for long-term scalable frost prevention

**Christian Machado[1]†, Benjamin Stern[1]†, Haiyue Huang[2], Asma Ul Hosna Meem[1], Jiaxing Huang[3,4], Kyoo-Chul Kenneth Park[1]***

**Antifrosting surfaces are critical to the efficient and safe operation of infrastructure in cold and humid environments where deposition of frost (porous ice) is thermodynamically inevitable. Such infrastructure can include above-ground power cables and outdoor heat pumps. Here, we introduce a hybrid surface design that passively controls the diffusion of water vapor over a surface to sustain flat frost-free regions for long periods of time. We report more than 150 hours (~1 week) of frost prevention for a single hybrid unit cell, which is three orders of magnitude longer than reported frosting onset for other state-of-the-art techniques. We then demonstrate the potential for large-area frost prevention by scalable tessellation of unit cells and an intrinsic durability to scratches/cracks and physical contamination.**

## INTRODUCTION

Condensation frosting is a dominant mode of porous ice accumulation in cold and humid environments, induced when a supersaturation of water vapor is present near a surface cooled below water's freezing point (*1*, *2*). This supersaturation indicates a relative humidity (*RH*) local to the surface greater than 100%, where $P/P_{\mathrm{sat,liq}} > 1$ for vapor partial pressure $P$ and saturation pressure of liquid water $P_{\mathrm{sat,liq}}$ at the surface temperature ($T_s$) (*3*). Many critical infrastructures are required to operate under such frosting conditions and are vulnerable to damage or performance degradation, including power lines (*4*, *5*), vehicle sensors (*6*, *7*), and heat exchangers used for cooling and refrigeration (*8*–*10*). Mechanical damage and inefficient thermal transport through the frost layer, among other detriments, can result in tremendous costs and safety hazards (*5*, *11*, *12*). For example, the 2021 Texas power crisis resulted from more than 5 days of frosting/icing and extreme cold conditions, affecting 4.5 million households (*12*, *13*). Development of robust and long-lasting antifrosting techniques is therefore vital to prevent costly mechanical failures, energy inefficiencies, and safety hazards.

Current research efforts have yielded mechanisms for passive frost resistance by altering surface chemistry and topography to generate nonwetting surfaces (*14*–*18*) or lubricant-infused surfaces, such as slippery liquid infused porous surfaces (SLIPS) (*19*–*21*), which delay the onset of frosting. Nanoengineered surfaces containing hygroscopic liquids have also demonstrated ability to delay frosting onset by overlapping humidity sink regions (*22*). Ice removal techniques have also shown promise, such as low interfacial toughness (LIT) surfaces for passive shedding of densely-packed ice (*23*) and low-adhesion surfaces like SLIPS (*21*, *24*). However, each technique functions with some limitations; for example, large surface areas are generally required for LIT deicing (*23*), and SLIPS lose their function as the lubricating layer depletes (*24*–*26*). Furthermore, reported nonwetting, lubricant-infused, or hygroscopic-engineered surfaces that delay frosting onset cannot maintain frost-free regions longer than 0.1 to 5 hours (*15*, *20*, *21*, *27*). Some recent findings suggest that strategic spatial control of frosting may help promote more stable frost-free regions by use of polyelectrolyte coatings, micropillars, or macrotextures; however, the size and geometries of these frost-free regions can be limited (e.g., macrotextures typically require a concave frost-free region) (*28*–*30*).

Antifrosting surfaces must also be durable to scratches and contamination when operating in real environments. For example, many nonwetting surfaces are vulnerable to damage of the micro/nanotextures that induces a marked increase in ice adhesion by mechanical interlocking, or lubricant depletion for SLIPS (*15*, *21*, *24*, *26*). Furthermore, both scratches and physical contaminants can provide undesired sites for water nucleation, including capillary condensation at humidities that would otherwise not favor any phase change (*3*, *31*, *32*).

In this work, we demonstrate a hybrid technique to achieve highly stable and spatially scalable frost-free regions, with intrinsic scratch/crack- and contamination-resistant attributes. To achieve long time spans of frost resistance ($t > 150$ hours ~1 week), we control the spatial frost distribution such that targeted areas experience a local suppression of the degree of supersaturation, and these areas are coated in a hygroscopic material which is highly frost resistant at these lower supersaturations. Specifically, we combine millimeter-scale macrotextures with the two-dimensional (2D) material graphene oxide (GO), which exert control on the vapor diffusive flux in a complementary manner to allow the flat GO surface to remain frost free for extended periods of time. To demonstrate the synergistic antifrosting effects of the hybrid design approach, we selected GO as a model material because of its exceptional hygroscopic properties, with water vapor uptake rates twice that of silica gel (*33*, *34*), and the observed ability to resist frosting of the exposed surface. Furthermore, researchers Zokaie and Bai, among others, have suggested GO has an intrinsic ability to suppress freezing of intercalated water molecules by nanoconfinement effects (*35*–*38*). We use bulk structures of GO, in the form of moldable doughs, which contain the critical nanoscale interstitial spaces to confine adsorbed water molecules while maintaining a frost-free outer surface. By using a hybrid

---

[1]Department of Mechanical Engineering, Northwestern University, Evanston, IL 60208, USA. [2]Division of Physical Sciences, College of Letters and Science, University of California, Los Angeles, CA 90024, USA. [3]Department of Materials Science and Engineering, Northwestern University, Evanston, IL 60208, USA. [4]Department of Materials Science and Mechanical Engineering, Westlake University, Hangzhou, Zhejiang, PR China.
*Corresponding author. Email: kpark@northwestern.edu
†These authors contributed equally to this work.

Downloaded from https://www.science.org at Northwestern University on October 30, 2024

macrotexture-GO design, we report unprecedented week-long frost prevention on a flat surface (100% frost-free)—a substantial outperformance of the current state-of-the-art antifrosting techniques.

### Condensation frosting on hybrid macrotexture-GO surfaces

As shown in Fig. 1, the condensation frosting process on any surface can be characterized into three stages, occurring sequentially after some initial time point $t_0$ when the surface is fully dry: ($t_0 \longrightarrow t_1$) Water vapor condenses into liquid on the surface; ($t_1 \longrightarrow t_2$) liquid water freezes into porous ice (frost); ($t_2 \longrightarrow t_3$) established frost grows perpendicular to the surface as vapor desublimates at the solid-vapor interface, termed "out-of-plane" frost growth (*1*).

We see in the top row of Fig. 1 that a flat, untreated surface frosts uniformly within the $t_2$ time span; however, our goal is to resist frosting for times $t >> t_3$. We achieve this by first introducing a millimeter-scale texture to the surface (Fig. 1, center row) and then coating the central flat valley in a GO dough (Fig. 1, bottom row). Here, all frosting is constrained to the texture peaks while leaving the flat valley frost free, owing to the diffusion-focusing effect of the macrotextures (*30*, *39*). This frosting at the peaks is therefore sacrificial and can be taken as a thermodynamic inevitability for any surface that attempts to resist frosting for very long times (*28*–*30*).

Frosting experiments in Fig. 1 contrast the macrotexture-GO frost resistance (bottom-right) with an uncoated macrotextured surface (center-right). These experiments are performed in an environmental chamber where the far-field pressure $P$ is set by a humidity controller and the surface is cooled by an internal coolant flow (see fig. S1). We define the supersaturation condition for an experiment as $P/P_{\mathrm{sat,liq}}$ (*2*, *40*). The experiments in Fig. 1 are conducted at $T_s = -12°\mathrm{C}$ and $P/P_{\mathrm{sat,liq}} = 3.9$ and serve as a characteristic demonstration of the necessity of a GO (or similarly functional material) coating to prevent frosting on the flat valley of a macrotextured surface. Note that this surface temperature is maintained for all reported experiments unless indicated otherwise.

Experiments in fig. S2 demonstrate that the enclosed macrotexture does perform better than macrotextures that are not enclosed and can achieve a frost-free valley under less extreme supersaturation conditions ($P/P_{\mathrm{sat}} = 2$ in this case). However, the valley will form frost under sufficiently high supersaturation as exhibited in Fig. 1 for $P/P_{\mathrm{sat}} = 3.9$. Increasing the valley size $d$ would achieve a similar effect as increasing the supersaturation, which is shown in fig. S3. Similarly, fig. S4 demonstrates that GO doughs can resist frost without any macrotexture for several hours at moderate supersaturation (e.g., $P/P_{\mathrm{sat,liq}} = 3.1$) but not for times exceeding 3 hours at increased supersaturation ($P/P_{\mathrm{sat,liq}} = 3.6$).

## RESULTS

### Hybrid antifrosting mechanism

The long-term stability of the flat frost-free region is achieved by a hybrid mechanism for diffusion-flux control, which is diagrammed in Fig. 2A. The influence of the GO and macrotexture

Downloaded from https://www.science.org at Northwestern University on October 30, 2024

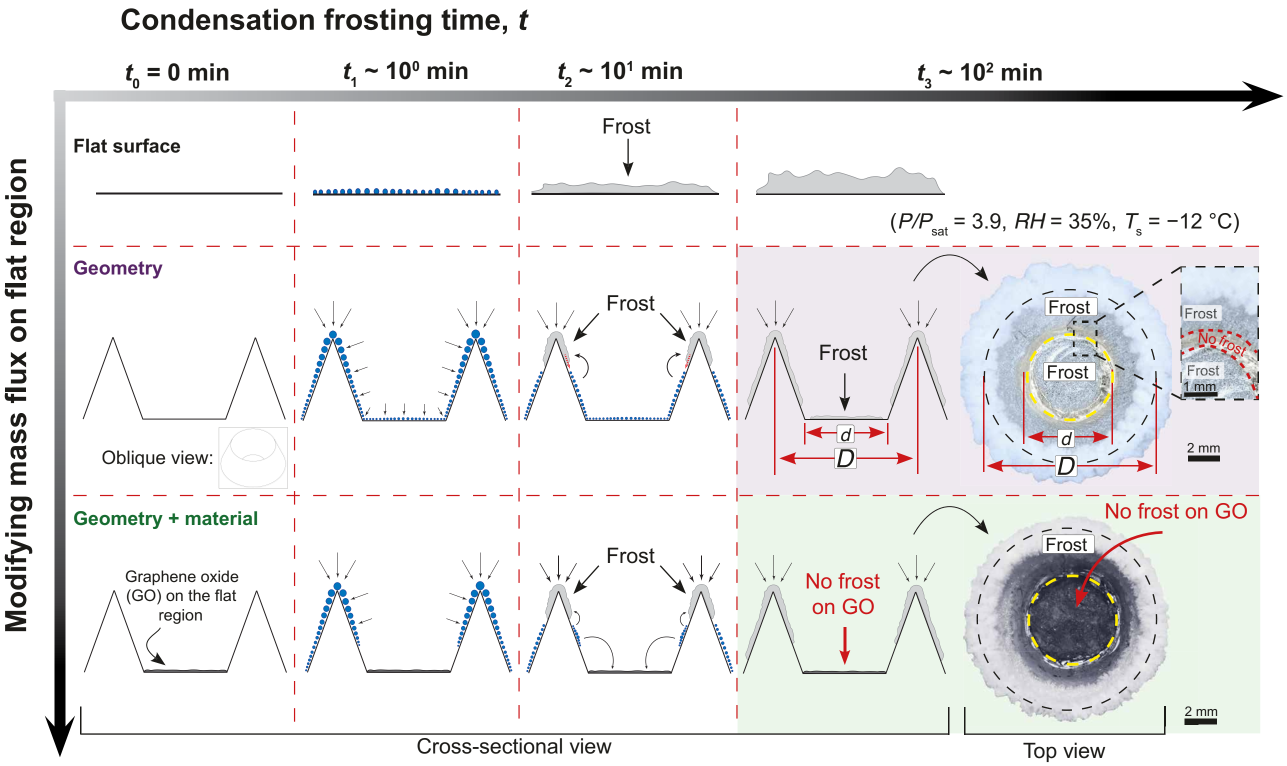

**Fig. 1. A schematic of the design methodology for this study.** To achieve long-term frost prevention on a flat surface, we consider the role of macroscale geometry (unit cell) and GO material. The demonstrative macrotexture geometry resembles an inverted truncated cone, characterized by a peak-to-peak distance $D$ and valley diameter $d$ = 5 mm. A GO dough is then applied as a thin coating to the valley (thickness ≈ 600 μm). The macrotexture serves to focus the diffusion of water vapor to the texture peaks ($t_1$), such that frost nucleates at the peak regions first because of the larger mass of supercooled water and then propagates toward the valley ($t_2$) (*32*). Experiments ($t_3$) depict no frost on the GO-coated valley surface but frost on the uncoated valley surface after $t$ = 3 hours.

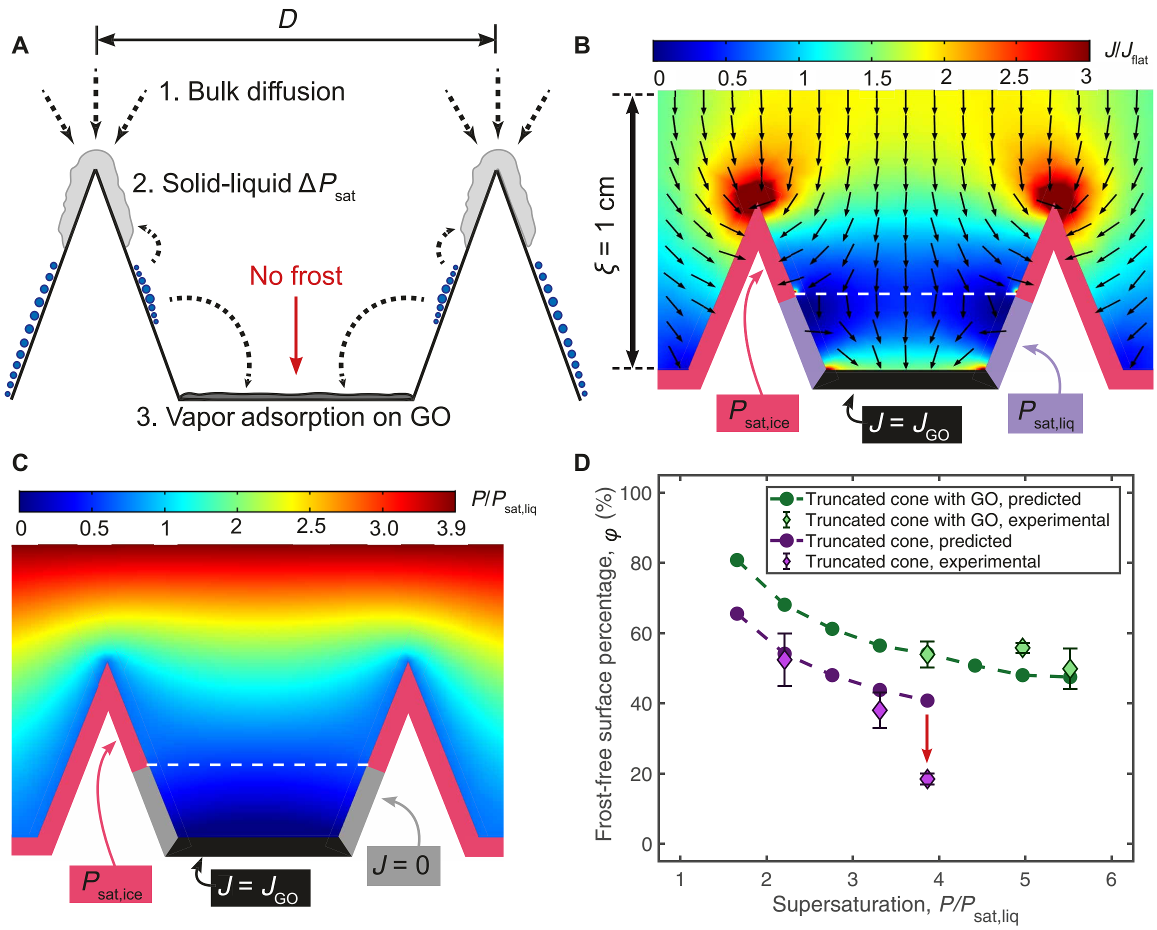

**Fig. 2. Modeling the physical mechanisms for vapor flux control that allows for prediction of antifrosting performance.** (**A** to **C**) Cross-sectional views of the hybrid macrotexture-GO surface. (A) Schematic of the three main types of vapor flux on the hybrid surface. (B) Simulated diffusion flux field over the 3D surface domain, normalized by the flux magnitude on a flat surface. A flux boundary condition is applied to the GO valley, taken from the measurements reported in fig. S5. (C) Simulation of the partial pressure of water vapor around the hybrid surface domain. There is an apparent region of strong undersaturation in the valley (dark blue color) that emphasizes the long-term frost-free stability while the GO absorbs moisture from the air. (**D**) Predictions of the frost resistance for a macrotextured surface without GO (purple) and with GO (green) are plotted alongside experimental measurements. Total projected frost-free surface percentage at $t = 3$ hours is calculated as $\varphi = A_{unfrosted}/\pi(D^2/4)$. The red arrow indicates a deviation between simulated and experimental results for the case without GO at high supersaturation ($P/P_{sat,liq} = 3.9$), due to the formation of multiple frost fronts (see Fig. 1, center-right).

on the diffusion flux field are characterized by three critical interactions: (i) focused diffusion from the bulk air mass onto the macrotexture peak (*30*, *39*, *41*), (ii) the ice-water interaction on the macrotexture walls, and (iii) the vapor adsorption into the GO dough. During the $t_2$ time span, the ice and GO factors particularly influence the dynamic frosting on the macrotexture walls. Specifically, some portion of the wall remains dry and frost free, characterized by a stable location of the ice-water boundary (i.e., frost front), and the location of this frost front is determined by the interplay between the GO and frost regions. Both frost and GO are hygroscopic materials, and so nearby water droplets readily evaporate and diffuse into the closest of these materials, indicated by the curved dotted arrows in Fig. 2A. In the case of ice, this hygroscopic ability is driven by a difference in the saturation vapor pressure compared to liquid water, $\Delta P_{sat} = P_{sat,liq} - P_{sat,ice} > 0$ (*28*, *30*, *40*). Once all nearby droplets have evaporated, the frost front is unable to propagate by direct ice bridging and has effectively "stalled," leaving the remainder of the macrotexture wall frost free.

The simulated diffusion flux field in Fig. 2B depicts the three key interactions illustrated in Fig. 2A, where color gives the flux magnitude and arrows give the flux directions. Ice and liquid water boundaries are given by saturation pressures calculated from the Clausius-Clapeyron relation (*40*, *42*). The flux boundary condition on the GO surface is taken from the measurement in fig. S5 as $J \sim 10^{-3}$ mol/m$^2$·s. This simulation is used to predict the location of the stalled frost front (the dotted white line) taken as the point where all flux arrows along the liquid water domain (purple) point away from the wall, indicating evaporation of all liquid droplets (see fig. S6). We then use the predicted stable frost front location to plot the vapor pressure field in Fig. 2C. Pressure values are normalized by $P_{sat,liq}$ such that values $P/P_{sat,liq}$ near the cooled surface are exactly equal to the local *RH* at that point. The combined hygroscopic properties of ice and GO results in the dark blue region of undersaturation near the valley where $P/P_{sat,liq} << 1$, indicating strong frost resistance.

The stable liquid-ice boundary condition given in Fig. 2B is used to predict the unfrosted area of the hybrid unit cell. For varying

Downloaded from https://www.science.org at Northwestern University on October 30, 2024

supersaturation conditions, this liquid-ice boundary will change location on the sidewall, and so it is useful to define a frost-free percentage that captures this behavior and can be used to validate the simulation prediction. We define a frost-free surface percentage as the ratio of projected areas across the 3D unit cell

$$\varphi(\%) = \frac{A_{\text{unfrosted}}}{A_{\text{total}}} \times 100 \qquad (1)$$

where $A_{\text{unfrosted}}$ is a function of the supersaturation condition $P/P_{\text{sat,liq}}$ for a given surface temperature, and $A_{\text{total}}$ is the total unit cell area [$A_{\text{total}} = \pi(D^2/4)$ for the truncated cone unit cell]. Predicted φ values for the hybrid unit cell are plotted in Fig. 2D (green) with corresponding experimental measurements ($t$ = 3 hours) that provide validation for the simulation method. Simulation and experiment results for the macrotexture without GO are plotted in purple. The hybrid cell demonstrates a higher frost-free percentage than the case without GO for all $P/P_{\text{sat,liq}}$ due to the strong GO adsorption flux that further suppresses the vapor concentration in the valley, causing increased liquid evaporation on the walls. A simulation comparison between cases with and without GO is given in fig. S7, and close inspection of Fig. 2B confirms there is an increased flux magnitude at the GO edges where nearby liquid evaporates and is adsorbed into the GO (red color).

For sufficiently high $P/P_{\text{sat,liq}}$, there is a discrepancy between the predicted and experimental φ values for surfaces without GO (purple), indicated by the red arrow. This results from an independent nucleation and frost-propagation phenomenon on the valley surface, which is not captured by the simulation. Such frosting events could occur on the valley floor or sidewalls and can result from a variety of mechanisms, including capillary condensation, desublimation, or slight pressure fluctuations (*40*, *43*). The GO-coated samples, however, do not exhibit this frosting and thus validate the simulation up to supersaturation $P/P_{\text{sat,liq}} = 5.5$ (at least). To maintain a frost-free GO surface, the GO dough must remain undersaturated (i.e., the adsorption flux is maintained) during which time it is observed to not frost (Figs. 1 and 2 and fig. S4). When enclosed within a macrotexture, the suppressed supersaturation condition extends the GO saturation time far past the time it takes for an uncoated surface (no GO) to frost (fig. S7). Thus, not only does Fig. 2D confirm a stark improvement in the spatial antifrosting metric φ for GO-coated samples, but the onset time of frosting is extended markedly as well.

## Long-term antifrosting and spatial control

The long-term stability of the hybrid antifrosting mechanism is a direct result of the synergistic relationship between the macrotexture and GO design components. That is, the GO allows for an extended planar frost-free region between macrotexture features, and the macrotexture extends the GO saturation time for $t >> t_3$, allowing for a flat and highly stable frost-free valley surface. To that end, in Fig. 3 (A and B), we demonstrate over 150 hours (~1 week) of frost prevention on the valley surface.

To examine the stability of the frost-free valley, we define a new figure of merit

$$\varphi_{\text{flat}}(\%) = \frac{A_{\text{flat,unfrosted}}}{A_{\text{flat}}} \times 100 \qquad (2)$$

where $A_{\text{flat}} = \pi d^2/4$. This flat frost-free percentage is also useful to characterize other reported antifrosting techniques on exclusively flat surfaces, where in Fig. 3A, we provide a comparison between $\varphi_{\text{flat}}$ for the hybrid macrotexture-GO surface with SLIPS and superhydrophobic surfaces, as reported by Kim *et al.* (*21*), over a log-time scale. Characteristic $\varphi_{\text{flat}}$ values and frosting onset times for these different surfaces are also reported in table S1. Notably, the hybrid surface retains $\varphi_{\text{flat}} = 100\%$ for ~1000 times longer than the other techniques, which experience a frosting onset in $t < 20$ min (*21*, *28*). Superhydrophobic surfaces are then seen to frost entirely in $t = 100$ min, and SLIPS frost-free percentage drops to $\varphi_{\text{flat}} = 36\%$ in $t = 300$ min.

Images of the hybrid surface from this long-time frosting experiment are shown in Fig. 3B, where after 1 week in frosting conditions, all frost formation is constrained to the sacrificial macrotexture peaks, while the GO surface remains frost free. We expect the frosting onset time of the hybrid surface valley to far exceed 1 week, whereas other state-of-the-art techniques frost completely within hours. Thus, the macrotexture-GO design shows promise for solving a previously intractable problem: long-time frost resistance in high-supersaturation conditions.

To confirm the superior performance of the hybrid macrotexture-GO surface, we also demonstrate frosting of macrotextured hybrid unit cells with different valley coatings in fig. S8, including SLIPS, superhydrophobic chemical treatment (FS100), and thermally insulating polydimethylsiloxane (PDMS). This experiment demonstrates the superior performance of the GO surface coating, as all other surfaces begin frosting in 25 min at high supersaturation while the GO remains unfrosted.

Given the demonstrated long-term antifrosting performance of the hybrid unit cell, it is advantageous to then maximize the flat frost-free area of a given unit cell. We can achieve this by using vertical macrotexture walls, rather than the sloped walls of the truncated cone. This way, only the top face of the wall contributes to the projected flat area, which effectively removes the dependence of φ on the frost front location on the sidewall (Fig. 2). By making the wall thin, we can maximize the portion of flat area coated in GO, thereby maximizing φ. This design comparison is given in Fig. 3C, where the predicted frost-free percentage for a unit cell with thin vertical walls (blue) and a truncated cone unit cell (green) are plotted across a range of supersaturations. We see here that φ for a vertical-walled unit cell is constant for all $P/P_{\text{sat,liq}}$, while φ for the truncated cone unit cell decreases with $P/P_{\text{sat,liq}}$. In both cases, the GO remains unfrosted, and so $\varphi_{\text{flat}} = 100\%$.

We examine the antifrosting performance of a hexagonal unit cell in Fig. 3C, corresponding to the experiment in Fig. 3D and movie S1 (dimensions given in fig. S8B). The frost distribution across a pattern of hexagonal cells after 3 hours is depicted, where the hybrid macrotexture-GO unit cell is outlined in black dashed lines. The bottom-left cell (blue color) contains PDMS as a control material with similar thermal conductivity as GO, and the remaining metallic cells contain untreated aluminum. Only the cells containing GO remain unfrosted after 3 hours in $P/P_{\text{sat,liq}} = 3.4$ conditions. Notably, the high frost-free percentage φ = 89% of the hybrid GO-hexagon unit cell in this experiment is exactly equal to the percentage of total projected cell area, which is composed of flat valley. Conversely, only 28% of the total truncated cone projected area is composed of the flat valley, which contributes to the lower frost-free percentage at similar supersaturation in Fig. 3C.

We can achieve larger frost-free areas with patterns of hexagonal hybrid cells, as demonstrated using a polymer macrotextured surface in Fig. 3E and movie S2. Here, the combined flat valley area of four GO-coated cells remains unfrosted ($\varphi_{\text{flat}} = 100\%$, φ = 82%), while the

Downloaded from https://www.science.org at Northwestern University on October 30, 2024

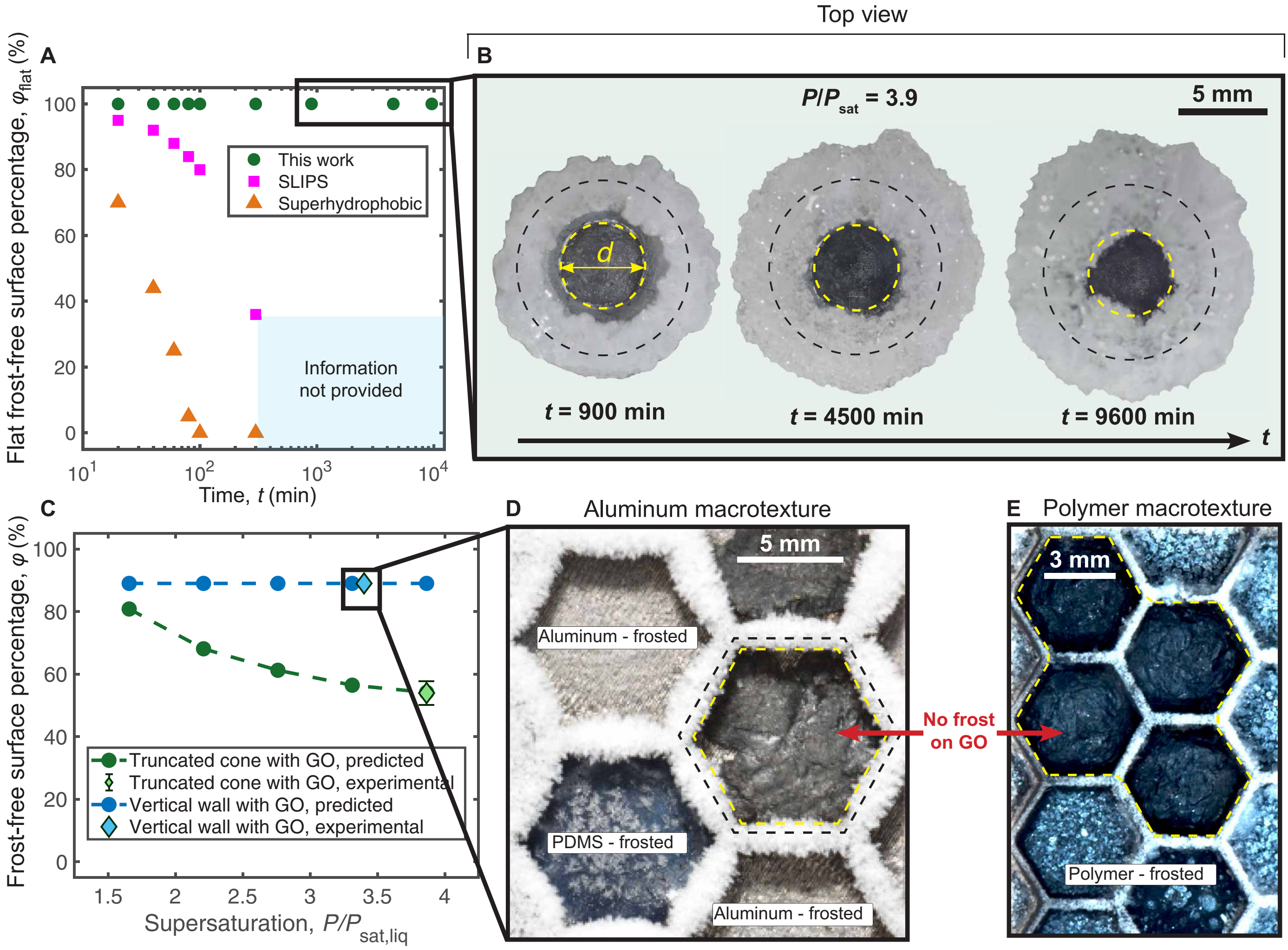

**Fig. 3. A demonstration of week-long and scalable antifrosting.** (**A**) We compare frost-free surface percentage on a flat area between this study ($P/P_{\mathrm{sat,liq}} = 3.9$) and previous works ($P/P_{\mathrm{sat,liq}} = 3.2$) (*21*). $\varphi_{\mathrm{flat}} = A_{\mathrm{flat,unfrosted}}/\pi(d^2/4)$ for the hybrid GO-macrotexture surface. (**B**) The hybrid surface (GO thickness ≈ 625 μm) demonstrates stable frost resistance on the flat valley (yellow dashed circle) for over 150 hours (~1 week) at $P/P_{\mathrm{sat,liq}} = 3.9$. The black dashed circle indicates the macrotexture peak. (**C**) Comparison of the total unfrosted region φ of unit cells with thin, vertical macrotexture walls (blue) and sloped walls (green). The experiment at $P/P_{\mathrm{sat,liq}} = 3.4$ (green) corresponds with (B) and the experiment at $P/P_{\mathrm{sat,liq}} = 3.4$ (blue) corresponds with (D). (**D**) Hexagonal macrotextures (aluminum) after 3 hours in frosting conditions ($P/P_{\mathrm{sat,liq}} = 3.4$). The dashed black hexagon indicates a hybrid macrotexture-GO unit cell, and the dashed yellow hexagon indicates the flat frost-free valley. The bottom-left cell (blue) contains PDMS, which has similar thermal conductivity to GO. (**E**) Four GO-macrotexture unit cells (Anycubic resin) demonstrate scalable antifrosting ($P/P_{\mathrm{sat,liq}} = 3.4$, $t = 1.4$ hours). Hexagon walls (top view) are 3 mm tall in (D) and (E).

uncoated cells (polymer material) frost completely. Between Fig. 3 (D and E) and fig. S8, we see the versatility of this approach, where hexagon unit cells can be of different sizes and material (metal or polymer).

## Toward durable antifrosting

We next demonstrate the intrinsic durability of the hybrid macrotexture-GO surface, with respect to impacts by mesoscale scratches/cracks and contamination (feature size <1 mm) on antifrosting. Specifically, we identify the GO dough as the most potentially vulnerable component of the hybrid surface, as the millimeter-scale size of the macrotextures is much larger than the size of a mesoscale scratch or contaminant, but these sizes are comparable to the dimensions of the GO dough (5-mm disk, ≈600 μm thick). However, we hypothesized that the internal nano- and microstructures of the GO would resist damage by mesoscale features, such that only the topography and exposed surface area of the dough would be affected. The simulations in Fig. 4A (with macrotexture) and fig. S9 (no macrotexture) depict an undersaturated region near the scratched and contaminated GO. In Fig. 4A, the scratched/contaminated hybrid surface exhibits a strongly undersaturated valley region, similar to the pristine GO sample in Fig. 2C. Therefore, we can rationally expect similar vapor adsorption and frost-resistant characteristics of a scratched GO dough as a pristine sample, assuming sufficient exposed GO surface area.

The frosting experiment in Fig. 4B confirms the simulation result, as the cracked and contaminated GO surface remains 100% frost free after 15 hours in high-supersaturation conditions ($P/P_{\mathrm{sat,liq}} = 4.5$). We used spherical plastic particles (size ≈ 500 μm) to contaminate the GO dough during the fabrication process, such that several particles

Downloaded from https://www.science.org at Northwestern University on October 30, 2024

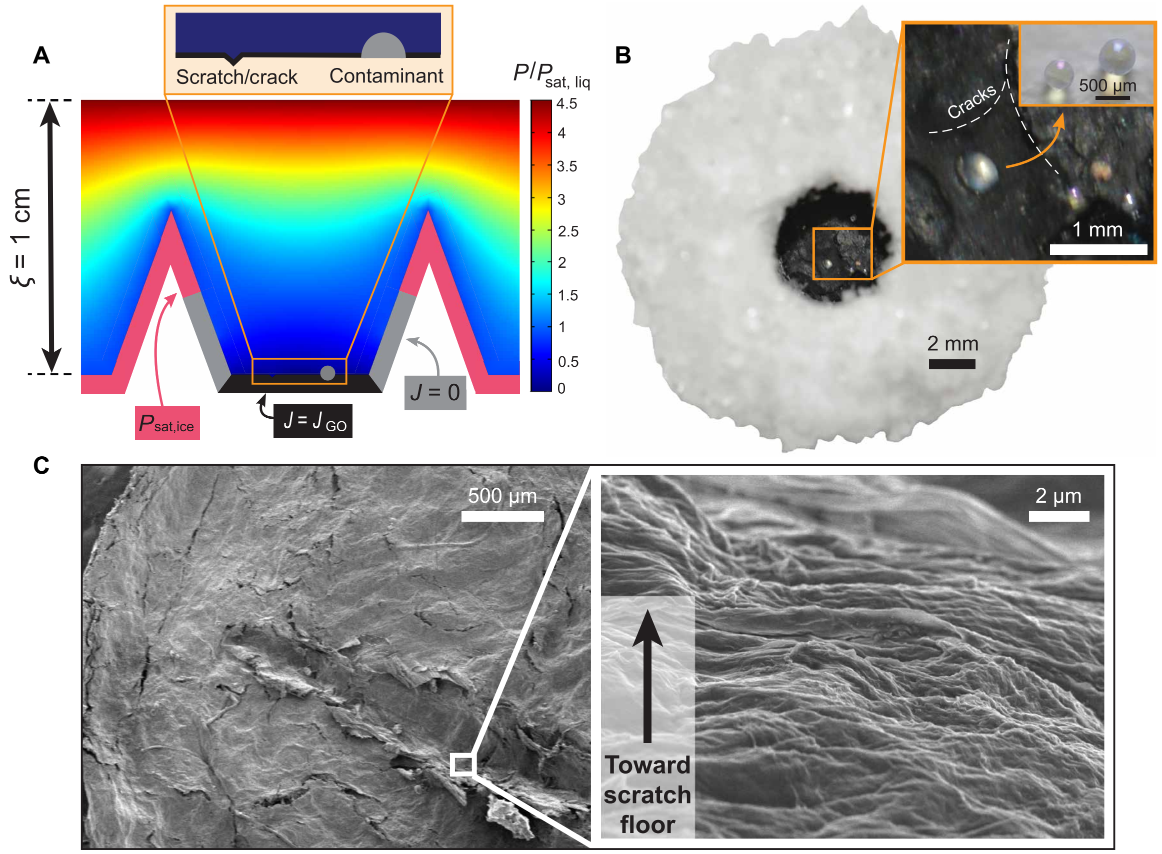

**Fig. 4. The hybrid GO-macrotexture surface that demonstrates scratch- and contamination-resistant antifrosting.** (**A**) Simulated concentration field over a hybrid surface where the GO dough contains a single scratch/crack (100-μm depth) and single spherical contaminant (500-μm diameter), for condition $P/P_{sat,liq} = 4.5$ (cross-sectional view). (**B**) A contaminated and cracked hybrid GO-macrotexture surface after 15 hours in extreme frosting conditions, $P/P_{sat,liq} = 4.5$ (top view). The GO dough (thickness ≈ 698 μm) is contaminated with spherical plastic particles and displays natural cracks on the dough surface. (**C**) SEM image of a GO dough with a single intentional scratch (depth = 97 ± 13 μm), where the magnified image (right) depicts a layered structure along the scratch inner wall. This intentionally scratched GO dough effectively resists frosting in a hybrid surface through the mechanism in (B) (see fig. S10).

are exposed to the humid environment during frosting. This result is consistent with other experiments like Fig. 3C that depict cracked and scratched GO doughs working effectively in the hybrid surface. The hypothesis is also supported by scanning electron microscopy (SEM) images from inside of a scratch on a GO dough surface (Fig. 4C) that depict a layered nanostructure as reported in the literature (*33*, *37*, *44*). The corresponding frosting experiment with this scratched GO sample is shown in fig. S10.

## DISCUSSION

We envision the hybrid macrotexture-GO surface as a robust antifrosting tool, with particularly strong application to cases requiring long passive antifrosting times. The versatility is exemplified by demonstrations of scalability using a hexagonal unit cell design in Fig. 3 (D and E). There are also opportunities to explore other nanoporous hygroscopic materials and optimize the macrotexture geometry, based on our rational hybrid design method. Furthermore, the intrinsic durability of the GO dough's intrinsic antifrosting ability to scratches/cracks and contamination promotes the effective fabrication and function of this technique in real environments; however, work remains to fully characterize the durability with a broad variety of contaminants. Application of the hybrid technique to real environments could also be enhanced by combining the hybrid surface with a deicing mechanism to remove the sacrificial frost on the macrotexture peaks (as seen in Figs. 3 and 4); for example, one could apply an LIT coating on the macrotexture peak to facilitate shedding of the dense coarsened ice which forms after many hours of frosting.

## MATERIALS AND METHODS

### Macrotexture sample preparation

Macrotextures resembling a truncated conical serration are 3D printed as hollow shells (Formlabs Form2, clear resin), such that an internal coolant flow will uniformly cool the texture surface (see fig. S1). The circular valley is designed with a diameter of 5 mm and the axisymmetric texture has a vertex angle of 40°. Hexagonal-patterned macrotextures with thin walls are 3D printed as solid structures, rather than as hollow shells. Hexagonal samples are either polymeric (Anycubic DLP, black resin) or aluminum (direct energy deposition). The specific design parameters, including vertex angle, height, and peak-to-peak distance, are all controlled using CAD (SolidWorks). Once printed, the hollow shells are covered with untreated 1100 aluminum sheets (51 μm, McMaster-Carr), adhered

Downloaded from https://www.science.org at Northwestern University on October 30, 2024

by thermally conductive copper tape (3M Scotch Double-Sided Conducted Copper Tape, Digi-Key Electronics). The aluminum is cleaned by sonicating with detergent (Alconox Alcojet Low Foaming Detergent, Thermo Fisher Scientific) for 30 min.

### GO sample preparation

GO aqueous dispersion (1% w/w, Standard Graphene, GO-V50) is diluted to 0.1% w/w with deionized water. The diluted suspension is then passed through a vacuum filtration apparatus using polymeric filter paper (0.22 μm, nitrocellulose, Merck Millipore). The thickness of the film is determined by the amount of GO dispersion used. To create GO dough, the dried GO films are kneaded with excess water to create a ball and then rolled out to the desired thickness (~600 μm). GO doughs are adhered directly using thermally conductive copper tape. Contaminated GO dough is prepared by combining small plastic particles into a hydrated dough by hand until dispersed throughout the dough. The plastic particles (Yaomiao, UV Resin Beads) are approximately spherical with diameter 500 ± 100 μm.

### Characterization of GO doughs

Doughs are left out overnight at ambient room conditions to dry. Dried doughs are imaged (Nikon D5500, 5× objective), and the thickness is measured using ImageJ. Scanning electron microscope images in Fig. 4 are taken with 2- to 3-kV accelerating voltage (EPIC SEM S4800), and samples are coated in osmium (7 to 10 nm thick). A laser confocal microscope (Olympus 3D, 10× objective) is used to measure the depth of a scratch in the dough surface (fig. S10).

### Superhydrophobic aluminum and SLIPS aluminum preparation

Aluminum foils (127 μm thick) are cleaned in a solution of Alcojet and deionized water and then made super hydrophilic by boiling for 30 min at 350°C to create a nanotextured boehmite layer. The foils are then submerged in a solution of fluoroaliphatic phosphate ester fluorosurfactant (FS100, Mason Chemical Company) at 70°C for 2 hours to render the surface superhydrophobic (and superoleophilic). SLIPS are created by spin-coating silicone oil (100 cst) on one side of the superhydrophobic foil for 2 min at 4000 rpm. The superhydrophobic and SLIPS foils are then cut into hexagon shapes and adhered to the desired hexagonal macrotextured surface with copper tape.

### Truncated cone macrotexture frosting experiments

The 3D-printed shell assembly is attached to a circulating chiller (VWR Refrigerated Circulating Bath) using 9.5-mm flexible plastic tubing. A 50:50 mixture of ethylene glycol and water is cooled and flows through the shell to uniformly cool the macrotextured surfaces. The shell assembly is mounted in a closed environmental chamber with a humidity controller (Electro-Tech Systems Humidity Controller), humidity sensor (E+E Elektronik), humidifier (BONECO), and dry air supply line. The humidifier is placed far away from the shell assembly to reduce the possibility of nonevaporated liquid droplets depositing on the surface (i.e., fog collection). During the cooling process, dry air is flowed into the chamber to reduce the humidity to near zero so that no condensation or condensation frosting will occur here. Once an equilibrium surface temperature has been reached [measured by a type K thermocouple (Fluke Instruments)], the chamber is immediately humidified to the desired relative humidity. A camera (Nikon D5500, Micro NIKKOR 105-mm lens) is placed outside the chamber and programmed to take interval images. These images are then evaluated in ImageJ to measure the size of the frost-free zone.

### Hexagonal macrotexture frosting experiments

Hexagonal-patterned macrotextures with thin walls are tested on a flat Peltier stage (Teca LCP Cascade), as an internal coolant flow would be unnecessary. The rest of the environmental control chamber is the same as depicted in Fig. 2. The Peltier stage is connected to a dc power supply, and the hot side is connected to an external heat sink that is then connected to the circulating chiller. The GO samples are cooled in a dry environment until the set point temperature is reached (measured by type K thermocouple probe), and then the humidity is rapidly increased. Images are taken at regular intervals (see the "Truncated cone macrotexture frosting experiments").

### GO adsorption flux measurements under frosting conditions

GO adsorption flux is measured by cooling the dough on a Peltier stage and weighing the sample over time to track the mass of adsorbed water. The Peltier stage is cooled to −5°C and set in 25% *RH*. Flux is assumed to be primarily dominated by the top dough face, which has much larger area than the edges. Error bars are given as the SD at each time point for five experiments.

### COMSOL Multiphysics simulations

The diffusive boundary layer was set at $\xi = 1$ cm, consistent with prior literature (*30*, *39*, *41*). The concentration boundary conditions are taken as the saturation vapor pressures of ice and supercooled water at −12°C, calculated from the Clausius-Clapeyron equation (*40*, *42*). The relative humidity was defined at an ambient chamber temperature of 22°C.

The early-stage frosting dynamics on the truncated conical macrotexture are captured by the flux simulation in Fig. 2B. The frost front location is given by the boundary between liquid and ice concentration boundary conditions, which is dictated by the transition in flux direction indicated by black arrows in plots Fig. 2B and fig. S6. These equilibrium boundary conditions are then applied to simulations of the water vapor concentration normalized by the saturation concentration of water at the surface temperature ($P_{\mathrm{sat,liq}}$) to determine the antifrosting stability of the valley surface (Fig. 2C). At this later time point, it is assumed that the entirety of the liquid region becomes evaporated and then is treated as a zero-flux boundary, as observed in experiment. In Fig. 4 and fig. S8, we simulate the scratch and contaminant as geometric features of the GO surface, concave and convex respectively, where the contaminant has a zero-flux boundary condition and the scratch walls have the same flux boundary condition as the rest of the GO surface (fig. S5).

## Supplementary Materials

**The PDF file includes:**

Figs. S1 to S10
Table S1
Legends for movies S1 and S2

**Other Supplementary Material for this manuscript includes the following:**

Movies S1 and S2

## REFERENCES AND NOTES

1. N. H. Fletcher, *The Chemical Physics of Ice* (1970).
2. S. F. Ahmadi, J. B. Boreyko, "Condensation frosting" in *Ice Adhesion: Mechanism, Measurement and Mitigation*, K. L. Mittal, C.-H. Choi, Eds. (Wiley, 2020), pp. 111–134.

Downloaded from https://www.science.org at Northwestern University on October 30, 2024

3. D. Beysens, Dew nucleation and growth. *C. R. Phys.* **7**, 1082–1100 (2006).
4. J. L. Laforte, M. A. Allaire, J. Laflamme, State-of-the-art on power line de-icing. *Atmos. Res.* **46**, 143–158 (1998).
5. S. E. Chang, T. L. McDaniels, J. Mikawoz, K. Peterson, Infrastructure failure interdependencies in extreme events: Power outage consequences in the 1998 Ice Storm. *Nat. Hazards* **41**, 337–358 (2007).
6. J. K. James, Classification of LIDAR sensor contaminations with deep neural networks, in *Proceedings of the Computer Science in Cars Symposium* (*CSCS*) (2018), vol. 8.
7. J. Park, N. V. Quach, Y. Kim, R. H. Cheng, M. Jenco, C. Yin, A. K. Lee, Y. Won, Machine learning analysis of autonomous vehicle sensors under extreme conditions in Alaska. *J. Electron. Packag. Trans. ASME* **145**, 044501 (2023).
8. W. M. Yan, H. Y. Li, Y. J. Wu, J. Y. Lin, W. R. Chang, Performance of finned tube heat exchangers operating under frosting conditions. *Int J Heat Mass Transf* **46**, 871–877 (2003).
9. K. S. Boyina, A. J. Mahvi, S. Chavan, D. Park, K. Kumar, M. Lira, Y. Yu, A. A. Gunay, X. Wang, N. Miljkovic, Condensation frosting on meter-scale superhydrophobic and superhydrophilic heat exchangers. *Int. J. Heat Mass Transf.* **145**, 118694 (2019).
10. J. Cui, W. Z. Li, Y. Liu, Y. S. Zhao, A new model for predicting performance of fin-and-tube heat exchanger under frost condition. *Int. J. Heat Fluid Flow* **32**, 249–260 (2011).
11. J. Yu, H. Zhang, S. You, Heat transfer analysis and experimental verification of casted heat exchanger in non-icing and icing conditions in winter. *Renew. Energy* **41**, 39–43 (2012).
12. S. Yang, C. Wu, G. Zhao, J. Sun, X. Yao, X. Ma, Z. Wang, Condensation frosting and passive anti-frosting. *Cell Rep. Phys. Sci.* **2**, 100474 (2021).
13. J. W. Busby, K. Baker, M. D. Bazilian, A. Q. Gilbert, E. Grubert, V. Rai, J. D. Rhodes, S. Shidore, C. A. Smith, M. E. Webber, Cascading risks: Understanding the 2021 winter blackout in Texas. *Energy Res. Soc. Sci.* **77**, 102106 (2021).
14. L. Cao, A. K. Jones, V. K. Sikka, J. Wu, D. Gao, Anti-icing superhydrophobic coatings. *Langmuir* **25**, 12444–12448 (2009).
15. S. Farhadi, M. Farzaneh, S. A. Kulinich, Anti-icing performance of superhydrophobic surfaces. *Appl. Surf. Sci.* **257**, 6264–6269 (2011).
16. S. Jung, M. Dorrestijn, D. Raps, A. Das, C. M. Megaridis, D. Poulikakos, Are superhydrophobic surfaces best for icephobicity? *Langmuir* **27**, 3059–3066 (2011).
17. J. B. Boreyko, C. H. Chen, Self-propelled dropwise condensate on superhydrophobic surfaces. *Phys. Rev. Lett.* **103**, 184501 (2009).
18. K. K. Varanasi, T. Deng, J. D. Smith, M. Hsu, N. Bhate, Frost formation and ice adhesion on superhydrophobic surfaces. *Appl. Phys. Lett.* **97**, 234102 (2010).
19. K. Golovin, S. P. R. Kobaku, D. H. Lee, E. T. DiLoreto, J. M. Mabry, A. Tuteja, Designing durable icephobic surfaces. *Sci. Adv.* **2**, e1501496 (2016).
20. D. Chen, M. D. Gelenter, M. Hong, R. E. Cohen, G. H. McKinley, Icephobic surfaces induced by interfacial nonfrozen water. *ACS Appl. Mater. Interfaces* **9**, 4202–4214 (2017).
21. P. Kim, T. S. Wong, J. Alvarenga, M. J. Kreder, W. E. Adorno-Martinez, J. Aizenberg, Liquid-infused nanostructured surfaces with extreme anti-ice and anti-frost performance. *ACS Nano* **6**, 6569–6577 (2012).
22. X. Sun, K. Rykaczewski, Suppression of frost nucleation achieved using the nanoengineered integral humidity sink effect. *ACS Nano* **11**, 906–917 (2017).
23. K. Golovin, A. Dhyani, M. D. Thouless, A. Tuteja, Low-interfacial toughness materials for effective large-scale deicing. *Science* **364**, 371–375 (2019).
24. M. J. Kreder, J. Alvarenga, P. Kim, J. Aizenberg, Design of anti-icing surfaces: Smooth, textured or slippery? *Nat. Rev. Mater.* **1**, 15003 (2016).
25. J. D. Smith, R. Dhiman, S. Anand, E. Reza-Garduno, R. E. Cohen, G. H. McKinley, K. K. Varanasi, Droplet mobility on lubricant-impregnated surfaces. *Soft Matter* **9**, 1772–1780 (2013).
26. M. J. Kreder, D. Daniel, A. Tetreault, Z. Cao, B. Lemaire, J. V. I. Timonen, J. Aizenberg, Film dynamics and lubricant depletion by droplets moving on lubricated surfaces. *Phys. Rev. X* **8**, 031053 (2018).
27. Y. Wang, J. Xue, Q. Wang, Q. Chen, J. Ding, Verification of icephobic/anti-icing properties of a superhydrophobic surface. *ACS Appl. Mater. Interfaces* **5**, 3370–3381 (2013).
28. Y. Jin, C. Wu, Y. Yang, J. Wu, Z. He, J. Wang, Inhibiting condensation freezing on patterned polyelectrolyte coatings. *ACS Nano* **14**, 5000–5007 (2020).
29. S. F. Ahmadi, S. Nath, G. J. Iliff, B. R. Srijanto, C. P. Collier, P. Yue, J. B. Boreyko, Passive antifrosting surfaces using microscopic ice patterns. *ACS Appl. Mater. Interfaces* **10**, 32874–32884 (2018).
30. Y. Yao, T. Y. Zhao, C. Machado, E. Feldman, N. A. Patankar, K. C. Park, Frost-free zone on macrotextured surfaces. *Proc. Natl. Acad. Sci. U.S.A.* **117**, 6323–6329 (2020).
31. M. Yarom, A. Marmur, Vapor-liquid nucleation: The solid touch. *Adv. Colloid Interface Sci.* **222**, 743–754 (2015).
32. Y. Hou, H. J. Butt, M. Kappl, "Water and ice nucleation on solid surfaces" in *Ice Adhesion: Mechanism*, *Measurement and Mitigation*, K. L. Mittal, C.-H. Choi, Eds. (Wiley, 2020), pp. 55–85.
33. B. Lian, S. De Luca, Y. You, S. Alwarappan, M. Yoshimura, V. Sahajwalla, S. C. Smith, G. Leslie, R. K. Joshi, Extraordinary water adsorption characteristics of graphene oxide. *Chem. Sci.* **9**, 5106–5111 (2018).
34. V. V. Perera, N. L. Fernando, B. Nissanka, D. R. Jayasundara, In situ real time monitoring of hygroscopic properties of graphene oxide and reduced graphene oxide. *Adsorption* **25**, 1543–1552 (2019).
35. M. Zokaie, M. Foroutan, Confinement effects of graphene oxide nanosheets on liquid–solid phase transition of water. *RSC Adv.* **5**, 97446–97457 (2015).
36. S. Kyrkjebø, A. Cassidy, N. Akhtar, R. Balog, M. Scheffler, L. Hornekær, B. Holst, R. Flatabø, Graphene and graphene oxide on Ir(111) are transparent to wetting but not to icing. *Carbon* **174**, 396–403 (2021).
37. S. Cerveny, F. Barroso-Bujans, Á. Alegría, J. Colmenero, Dynamics of water intercalated in graphite oxide. *J. Phys. Chem. C* **114**, 2604–2612 (2010).
38. G. Bai, D. Gao, Z. Liu, X. Zhou, J. Wang, Probing the critical nucleus size for ice formation with graphene oxide nanosheets. *Nature* **576**, 437–441 (2019).
39. Y. Yao, J. Aizenberg, K. C. Park, Dropwise condensation on hydrophobic bumps and dimples. *Appl. Phys. Lett.* **112**, 151605 (2018).
40. S. Nath, J. B. Boreyko, On localized vapor pressure gradients governing condensation and frost phenomena. *Langmuir* **32**, 8350–8365 (2016).
41. Y. Zhao, D. J. Preston, Z. Lu, L. Zhang, J. Queeney, E. N. Wang, Effects of millimetric geometric features on dropwise condensation under different vapor conditions. *Int. J. Heat Mass Transf* **119**, 931–938 (2018).
42. L. A. Guildner, D. P. Johnson, F. E. Jones, Vapor pressure of water at its triple point: Highly accurate value. *Science* **191**, 1261 (1976).
43. Q. Yang, P. Z. Sun, L. Fumagalli, Y. V. Stebunov, S. J. Haigh, Z. W. Zhou, I. V. Grigorieva, F. C. Wang, A. K. Geim, Capillary condensation under atomic-scale confinement. *Nature* **588**, 250–253 (2020).
44. C. N. Yeh, H. Huang, A. T. O. Lim, R. H. Jhang, C. H. Chen, J. Huang, Binder-free graphene oxide doughs. *Nat. Commun.* **10**, 422 (2019).

**Acknowledgments:** We thank P. Tangade for experimental assistance. **Funding:** This work is partially supported by NSF grant CBET-2337118 and KIST grant 2E32527. **Author contributions:** Experimentation, analysis, and writing were performed by C.M. and B.S. Resources, experimentation assistance, and editing were provided by H.H., A.U.H.M., and J.H. Conceptualization was performed by C.M., J.H., and K.-C.K.P. **Competing interests:** C.M., B.S., A.U.H.M., and K.-C.K.P. are inventors on patent application no. 18/424,059 held/submitted by Northwestern University that covers frost-resistant surfaces with macrotextured periodic lattice structures. The other authors declare they have no competing interests. **Data and materials availability:** All data needed to evaluate the conclusions in the paper are present in the paper and/or the Supplementary Materials.

Submitted 3 June 2024
Accepted 24 September 2024
Published 30 October 2024
10.1126/sciadv.adq8525

Downloaded from https://www.science.org at Northwestern University on October 30, 2024